

Biased ensembles of pulsating active matter

William D. Piñeros and Étienne Fodor

Department of Physics and Materials Science, University of Luxembourg, L-1511 Luxembourg, Luxembourg

We discover unexpected connections between packing configurations and rare fluctuations in dense systems of active particles subject to pulsation of size. Using large deviation theory, we examine biased ensembles which select atypical realizations of the dynamics exhibiting high synchronization in particle size. We show that the order emerging at high bias can manifest as distinct dynamical states with either a finite or a vanishing size current. Remarkably, transitions between these states arise from changing the system geometry at fixed bias and constant density. We rationalize such transitions as stemming from a change in the packing configurations favored by the geometry. Specifically, we reveal that a master curve in the unbiased dynamics, correlating polydispersity and current, helps predict the dynamical state emerging in the biased dynamics. Finally, we demonstrate that deformation waves can propagate under suitable geometries when biasing with local order.

Introduction.—Active matter encompasses systems which constantly dissipate energy to sustain collective behaviors far from equilibrium. For instance, assemblies of self-propelled particles (SPPs) [1–3] yield nonequilibrium phenomena which have been extensively studied, such as a polarized collective motion [4, 5] and a phase separation without attractive interactions [6, 7]. Energy dissipation can also take other forms beyond motility, opening the door to novel physics beyond that of SPPs. For instance, in some biological tissues (e.g., epithelial [8], cardiac [9], and uterine [10] tissues), each cell can sustain periodic changes of shape, leading to the propagation of deformation waves. A recent model of pulsating active matter (PAM) has captured such waves in terms of densely packed particles whose sizes constantly pulsate [11]. In contrast with other models of deforming particles where waves have not been observed [12–15], PAM relies on synchronizing nearby sizes [11, 16–19]. In the absence of any synchronizing interaction, it is largely unclear under which conditions deformation waves could still potentially emerge.

Biased ensembles (BEs) offer the perfect toolbox [20] to search for waves in non-synchronizing PAM. Building on large deviation theory [21], BEs select the rare trajectories which (i) achieve some atypical statistics of a chosen observable, while (ii) deviating the least from the original, unbiased dynamics. In practice, BEs do not presume *how* the system should accommodate the constraints (i-ii). At a sufficiently large bias, the dynamics are given enough play to explore novel configurations, potentially yielding dynamical phase transitions [22–24]. Rare trajectories can actually be mapped into an effective dynamics [25–28], which constitute the optimal mechanism for stabilizing the phases selected by BEs. This connection between optimal control and large deviations has inspired novel strategies for material design [29, 30].

In active matter, BEs have already been used to unravel novel mechanisms for promoting collective effects [31]. For instance, in large deviations of SPPs [32–34], BEs have revealed that alignment effectively emerges from avoiding collisions between nearby particles, yield-

ing collective motion [35–37]. This collective motion contrasts with that of standard flocking models which require ad hoc aligning rules [5]. In a similar fashion, it is tempting to examine whether BEs of non-synchronizing PAM entail unexpected transitions, potentially uncovering novel pathways towards wave formation.

In this letter, we investigate the collective dynamics in BEs of dense assemblies of pulsating particles in a two-dimensional box [Fig. 1]. Starting from configurations without any synchronization, we reveal how biasing with a global order parameter promotes transitions towards various homogeneous states: cycles, arrest, and intermittent behavior. Remarkably, the packing constraint imposed by the box geometry, whose signature already holds in unbiased configurations, specifically selects one of the three ordered states under bias. Finally, we show that deformation waves can be stabilized for

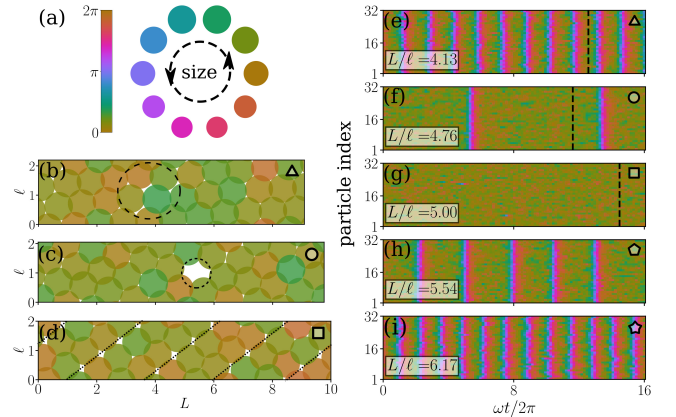


FIG. 1. (a) Particle sizes subject to periodic cycling. In biased ensembles at high density, changing the aspect ratio L/l results in various configurations with either (b) defects, (c) voids, or (d) regular structures. These correspond, respectively, to varying collective states as L/l varies: (e,i) cycles with periodic size change, (f,h) intermittent behavior with aperiodic size change, and (g) arrest with frozen size. Particles are indexed per increasing position along the L -axis. Dashed lines refer to the snapshots shown in (b)-(d).

specific geometries when biasing with a local order parameter. Overall, our results demonstrate that, at fixed bias and constant density, controlling the box geometry is a novel route towards unexpected phase transitions in BEs of PAM.

Pulsating active matter: The role of box geometry.— We consider a two-dimensional system of pulsating particles [Fig. 1] whose sizes change as

$$\sigma_i = \frac{\sigma_0}{2} \frac{1 + \lambda \sin \theta_i}{1 + \lambda}, \quad (1)$$

where $\sigma_0 = 1$ is the base size, θ_i the internal phase of particle i , and $\lambda = 0.05$ the pulsation amplitude. The particles follow overdamped Langevin dynamics:

$$\dot{\mathbf{r}}_i = -\mu_r \partial_{\mathbf{r}_i} V + \sqrt{2D_r} \boldsymbol{\xi}_i, \quad (2)$$

$$\dot{\theta}_i = \omega - \mu_\theta \partial_{\theta_i} V + \sqrt{2D_\theta} \eta_i. \quad (3)$$

The potential $V = \sum_{i,j < i} U(a_{ij})$ depends on the scaled distance $a_{ij} = |\mathbf{r}_j - \mathbf{r}_i| / (\sigma_i + \sigma_j)$, and $(\boldsymbol{\xi}_i, \eta_i)$ are uncorrelated Gaussian white noises with unit correlations. The diffusion coefficients $D_{r/\theta}$ and mobilities $\mu_{r/\theta}$ are set to unity, and the phase drift to $\omega = 10$. Interactions follow volume exclusion via a Weeks-Chandler-Anderson potential $U(a) = U_0(a^{-12} - 2a^{-6})$ with $U_0 = 1$ and cut-off set at $a = 1$. In contrast with [11], we do not consider here any synchronizing interaction between phases. In what follows, we run simulations with periodic boundary conditions for $N = 32$ particles at density $\rho = 1.6$ (unless stated otherwise), and we examine how the box aspect ratio L/ℓ [Fig. 1] impacts the emerging dynamics.

We start by evaluating the global order parameter:

$$\phi_{\text{gb}} = \frac{1}{N} \left(\sum_{i,j=1}^N \cos(\theta_i - \theta_j) \right)^{1/2}. \quad (4)$$

Configurations with a nearly uniform size distribution have $\phi_{\text{gb}} \simeq 1$, whereas those with high polydispersity have $\phi_{\text{gb}} \simeq 0$. Despite the absence of any synchronizing interaction, our simulations exhibit a moderate ordering of particle sizes. Indeed, the repulsion term in Eq. (3) constrains the sizes to fluctuate around a preferred value. This effect is captured at mean-field level by approximating $\partial_{\theta_i} V \approx (\partial_\varphi V)(\partial_{\theta_i} \varphi)$ [11]. The coefficient $\partial_\varphi V$ increases with ρ , and the packing fraction $\varphi = (\pi\rho/N) \sum_i \sigma_i^2$ admits the same local minimum for each $\theta_i \in [0, 2\pi]$, thus favoring order at high ρ .

Interestingly, we observe that $\langle \phi_{\text{gb}} \rangle$ (where $\langle \cdot \rangle$ indicates average over realizations) strongly varies with the aspect ratio L/ℓ , with a maximum at $L/\ell \simeq 5$ [Fig. 2(a)], showing that one can actually enhance order by appropriately tuning the box geometry. This enhancement is accompanied by a dynamical slowdown, as indicated by the reduction of the average phase current [Fig. 2(b)]:

$$\nu = \frac{1}{N\omega t} \sum_{i=1}^N \int_0^t dt' \dot{\theta}_i(t'). \quad (5)$$

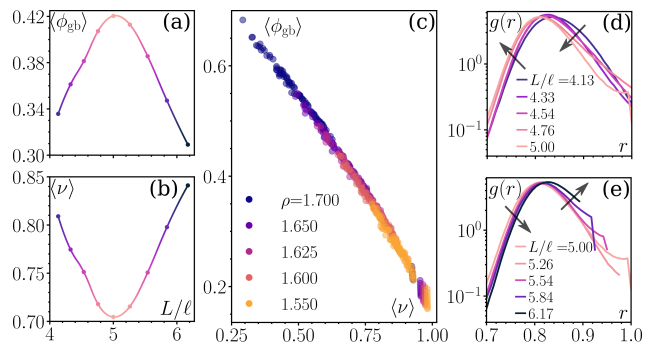


FIG. 2. (a-b) Global order $\langle \phi_{\text{gb}} \rangle$ and phase current $\langle \nu \rangle$ as functions of the aspect ratio L/ℓ . Lines are guides to the eye. (c) Correlation between global order $\langle \phi_{\text{gb}} \rangle$ and phase current $\langle \nu \rangle$ for various densities $\rho = N/(L\ell)$, changing both L/ℓ and the particle number N . (d-e) Radial distribution g as a function of the interparticle distance r . Arrows indicate increasing values of L/ℓ .

Similar results hold for other box ratios and particle numbers, see Fig. S4 in [38]. In fact, plotting $\langle \phi_{\text{gb}} \rangle$ against $\langle \nu \rangle$ for different values of N , L/ℓ , and ρ results in a master curve, where increasing order systematically correlates with decreasing current [Fig. 2(c)]. Interestingly, some of the curves, shown in Fig. 2(c) for different ρ , overlap. Indeed, for some combinations of N and L/ℓ , systems at various ρ can experience an equivalent average repulsion, yielding a similar set of values for $\langle \phi_{\text{gb}} \rangle$ and $\langle \nu \rangle$.

We can rationalize these results from a packing perspective. To this end, we evaluate the radial distribution function $g(r) = (1/N) \sum_{i,j \neq i} \langle \delta(r - |\mathbf{r}_i - \mathbf{r}_j|) \rangle$ for various L/ℓ . The first peak of g , whose position measures the averaged interparticle distance, progressively shifts, first to the left [Fig. 2(d)] and then to the right [Fig. 2(e)], as L/ℓ goes past the maximum of $\langle \phi_{\text{gb}} \rangle$ [Fig. 2(a)] and the minimum of $\langle \nu \rangle$ [Fig. 2(b)]. This result shows that particles are on average closer, experiencing higher repulsion, when the system orders and the dynamics slows down. Interestingly, one can actually identify a crystalline-like structure for the highest (lowest) value of $\langle \phi_{\text{gb}} \rangle$ ($\langle \nu \rangle$), see Fig. S1 in [38]: the box geometry here favors a more regular packing associated with higher order, lower polydispersity, and lower current. A similar effect takes place in passive, monodisperse systems where box geometry alters crystalline packing [39–41].

In short, our findings show that changing the box geometry alters the packing structure assumed by pulsating particles, which in turn provides a route to controlling order and current at fixed density in non-synchronizing PAM.

Ensembles biased by global order: Cycles and arrest.— We study the large deviations of the dynamics with respect to ϕ_{gb} [Eq. (4)]. In particular, we seek trajectories

for which the time average

$$\bar{\phi}_{\text{gb}} = \frac{1}{t_o} \int_0^{t_o} \phi_{\text{gb}}(t) dt \quad (6)$$

displays atypically large values at large observation time t_o . To this end, we use a BE selecting for such trajectories through rare realizations of the noise terms in Eqs. (2) and (3). Chiefly, we denote averages with respect to this BE as

$$\langle \cdot \rangle_{\text{gb}} = \frac{\langle \cdot e^{-sNt_o \bar{\phi}_{\text{gb}}} \rangle}{\langle e^{-sNt_o \bar{\phi}_{\text{gb}}} \rangle}. \quad (7)$$

The bias strength s effectively controls the statistics of $\bar{\phi}_{\text{gb}}$. At vanishing bias, $s = 0$, one recovers the ensemble of the original dynamics: $\langle \cdot \rangle_{\text{gb}} = \langle \cdot \rangle$. In this work, we implement the trajectory selection via a cloning algorithm using population dynamics [42]. It consists in simulating n_c identical (though distinctly seeded) parallel runs, which are regularly replicated/pruned through a sampling procedure parametrized by s . In the limit of large n_c and large t_o , this procedure converges to a BE whose trajectories represent the least unlikely dynamics to stabilize the desired atypical statistics of $\bar{\phi}_{\text{gb}}$.

For large N , numerical convergence becomes increasingly challenging [20]. Generally, a useful method consists in adding some terms in the dynamics which effectively approximate trajectory selection and improves convergence [20, 35, 36, 43, 44]. Here, we consider fully-connected synchronizing interactions:

$$\dot{\theta}_i = \omega - \mu_\theta \partial_{\theta_i} V + \varepsilon \sum_{j=1}^N \sin(\theta_j - \theta_i) + \sqrt{2D_\theta} \eta_i. \quad (8)$$

We adapt our numerical selection of trajectories [38] to ensure that, while using the dynamics in Eq. (8), we still sample the proper BE [Eq. (7)] defined independently of synchronizing interactions. Besides, for each run, we heuristically adjust the amplitude ε throughout the trajectory [38], which converges at large t_o to a value determined by s . In what follows, we are interested in the regime of bias which promotes order, namely atypically large $\bar{\phi}_{\text{gb}}$, corresponding here to $s < 0$ and $\varepsilon > 0$.

Starting from the unbiased configuration with highest $\langle \phi_{\text{gb}} \rangle$ and lowest $\langle \nu \rangle$, namely for $L/\ell \simeq 5$ [Figs. 2(a) and 2(b)], increasing $|s|$ yields a highly ordered state without phase current: $\langle \phi_{\text{gb}} \rangle_{\text{gb}} \simeq 1$ and $\langle \nu \rangle_{\text{gb}} \simeq 0$ [Figs. 3(a) and 3(b)]. Such a configuration is analogous to the arrested state previously reported in synchronizing PAM [11, 17]. Remarkably, considering an unbiased configuration at the tail of the curve $\langle \nu \rangle$ vs L/ℓ [Fig. 2(b)], increasing $|s|$ now yields an ordered state with non-vanishing averaged current [Figs. 3(a) and 3(b)], which is reminiscent of the cycling state in synchronizing PAM [11, 17]. Therefore, the box geometry not only impacts the unbiased dynamics of non-synchronizing PAM,

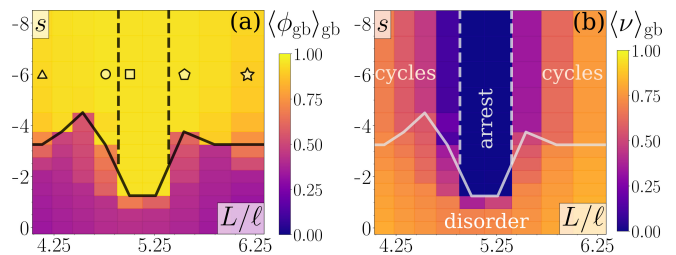


FIG. 3. Phase diagram in ensembles biased by global order [Eq. (7)] in terms of the bias strength s and the aspect ratio L/ℓ : (a) global order $\langle \phi_{\text{gb}} \rangle_{\text{gb}}$, and (b) phase current $\langle \nu \rangle_{\text{gb}}$. Boundary lines are for $\langle \phi_{\text{gb}} \rangle_{\text{gb}} = 0.65$ (solid) and $\langle \nu \rangle_{\text{gb}} = 0.1$ (dashed). Markers refer to various trajectories at $s = -6$, as shown in Fig. 1.

it also strongly influences its rare fluctuations, yielding two different types of ordered states.

Varying L/ℓ at constant $|s| > 4.5$, the transition between cycling and arrest [Fig. 3(b)] mirrors the slowdown of the unbiased dynamics [Fig. 2(b)]. Again, this result can be rationalized from a packing perspective. Specifically, arrest is associated with a regular packing [Fig. 1(d)] which impedes the periodic expansion and contraction of particles [Fig. 1(g)], whereas cycles have a defective packing [Fig. 1(d)] which facilitates global changes in particle sizes [Figs. 1(e) and 1(i)]. Note that $\langle \phi_{\text{gb}} \rangle_{\text{gb}}$ is slightly higher for arrest compared with cycles [Fig. 3(a)], so that regular packing is associated with a reduced polydispersity, as in the unbiased case [Fig. 2]. Interestingly, we also observe an intermittent dynamics with aperiodic size changes [Figs. 1(f) and 1(h)] whose packing contains motile voids [Fig. 1(c)]. Moreover, measurements of the radial distribution for each state dynamic state indeed further supports a clear structural difference between them, see Fig. S3 in [38].

Overall, our results for $(N, \rho) = (32, 1.6)$ show that packing configurations, imposed by the box geometry, impact both unbiased and biased dynamics. Importantly, we reveal that the unbiased statistics actually allows one to anticipate how the system orders as a function of L/ℓ in our BE. We find a similar effect is generically observed for other values of (N, ρ) ; for instance, see the phase diagram for $(N, \rho) = (26, 1.6)$ in Fig. S4 of [38].

Ensembles biased by local order: Deformation waves.— In synchronizing PAM [11, 17], deformation waves emerge as a competition between arrest and cycling. Given that in non-synchronizing PAM the BE promoting global order [Eq. (7)] yields arrest and cycles [Fig. 3], it is intriguing to understand what class of BE may also induce deformation waves. To this end, we introduce the local order parameter

$$\phi_{\text{lc}} = \frac{1}{N} \sum_{i=1}^N \sum_{j=1}^{n_i} \frac{\cos(\theta_j - \theta_i)}{n_i}, \quad (9)$$

where n_i is the number of neighbors in contact with par-

ticle i , and the corresponding biased average

$$\langle \cdot \rangle_{\text{lc}} = \frac{\langle \cdot e^{-sNt_o \bar{\phi}_{\text{lc}}} \rangle}{\langle e^{-sNt_o \bar{\phi}_{\text{lc}}} \rangle}, \quad \bar{\phi}_{\text{lc}} = \frac{1}{t_o} \int_0^{t_o} \phi_{\text{lc}}(t) dt. \quad (10)$$

To improve sampling, we now consider *locally* synchronizing interactions:

$$\dot{\theta}_i = \omega - \mu_\theta \partial_{\theta_i} V + \varepsilon \sum_{j=1}^{n_i} \sin(\theta_j - \theta_i) + \sqrt{2D_\theta} \eta_i. \quad (11)$$

In practice, Eq. (11) enhances convergence for the BE in Eq. (10) at moderate $|s|$, while Eq. (8) actually works better for the same BE at large $|s|$. At each s , we systematically compare results obtained by employing either type of interaction (i.e., with local or global synchronization), and select the ones with optimal convergence [38].

Interestingly, for values of L/ℓ coincident with the minimum of $\langle \nu \rangle$ [Fig. 2(b)], we observe again the emergence of an arrested state with local and global order [Figs. 4(a) and 4(b)] comparable to the results from the previous BE [Eq. (3)]. In contrast, for L/ℓ sufficiently far away from the minimum of $\langle \nu \rangle$, phase ordering now occurs through two distinct states. As $|s|$ increases, local order increases with negligible change in global order, i.e. $\langle \phi_{\text{lc}} \rangle_{\text{lc}} > \langle \phi_{\text{lc}} \rangle$ and $\langle \phi_{\text{gb}} \rangle_{\text{lc}} \simeq \langle \phi_{\text{gb}} \rangle$. In this state, particle sizes cycle periodically in a locally coordinated way, yielding the spontaneous emergence of deformation waves [Figs. 4(d) and 4(e)] not present in the unbiased dynamics [Fig. 4(c)]. For higher $|s|$, the range of particle coordination increases, which increases global order ($\langle \phi_{\text{gb}} \rangle_{\text{lc}} > \langle \phi_{\text{gb}} \rangle$) and ultimately results in a cycling state [Figs. 4(f)] similar to that of the previous BE [Fig. 1(e)].

In this manner, the BE promoting local order [Eq. (10)] reproduces all the states of synchronizing PAM [11, 17]: disorder, arrest, cycles, and waves. Furthermore, waves only arise for box sizes L accommodating at least one wavelength. As the wavelength increases with $|s|$, waves are only stable over a finite range of s . As such, waves can be seen as precursory to cycles. In contrast, arrest does not display such a gradual ordering from local to global, but rather directly emerges from disorder at comparatively low bias. Moreover, the critical s for this transition is almost unchanged when biasing with either global [Fig. 3(a)] or local [Fig. 4(b)] order.

In short, our results demonstrate that waves spontaneously emerge as a strategy to promote high *local* order, while maintaining only moderate *global* order. Again, the box geometry plays a crucial role here. Specifically, for values of L/ℓ promoting regular packing configurations, local deformations are strongly hampered, so that arrest is more stable than waves for any $s < 0$.

Discussion.—We reveal some unexpected connections between packing configurations and rare fluctuations in dense systems of pulsating particles. The box geometry is a proxy to controlling the packing structure, with

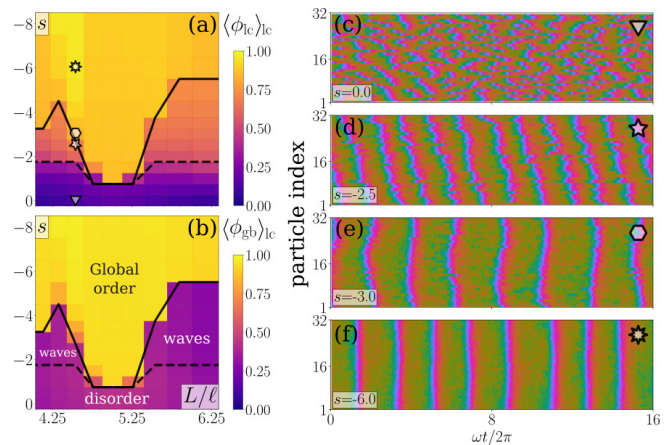


FIG. 4. Phase diagram in ensembles biased by local order [Eq. (10)] in terms of the bias strength s and the aspect ratio L/ℓ : (a) local order $\langle \phi_{\text{lc}} \rangle_{\text{lc}}$, and (b) global order $\langle \phi_{\text{gb}} \rangle_{\text{lc}}$. Boundary lines are for $\langle \phi_{\text{lc}} \rangle_{\text{lc}} = 0.65$ (solid) and $\langle \phi_{\text{gb}} \rangle_{\text{lc}} = 0.45$ (dashed). Markers refer to various trajectories at $L/\ell = 4.53$: (c) disorder, (d,e) waves, and (f) cycles.

dramatic consequences on collective effects. Specifically, we show that one can induce transitions between two types of ordered states in BEs, either with or without current, simply by changing the box geometry. Arrest is associated with regular packing configurations where the particle repulsion exactly counteracts their pulsation. Instead, when the box geometry induces a defective packing, it generates regions of inhomogeneous repulsion that ultimately lead to cycling.

Our transitions bring interesting parallels with the emergence of arrest in other dense systems. In densely packed SPPs, structural defects destabilize arrest [45], alter the glass transition [46], and induce intermittent plastic yielding [47]. The mechanical properties of such systems can actually be related to those of sheared granular systems [48]. Moreover, local growth of deforming particles also results in dynamical heterogeneities resembling sheared glasses [49]. These examples suggest that a generic mechanism may explain how activity controls the transitions between arrested and fluidized states. Remarkably, even in the absence of shear, allowing size fluctuations shifts the glass transition to lower temperatures [50, 51], illustrating how local deformation helps relax the dynamics near arrest [52].

Our approach could also motivate further studies in other active models where synchronization yields patterns [53–55]. For instance, considering BEs with local or global order could help delineate minimal conditions to stabilize patterns, similarly to how waves only emerge for specific box geometries in our case. To improve sampling, one could rely on more complex interactions beyond the synchronization considered here. To this end, recent methods inspired by machine learning provide a rich toolbox [56–58] which could prove quite useful.

We acknowledge insightful discussions with Y.-E. Keta and R. L. Jack. Work funded by the Luxembourg National Research Fund (FNR), grant reference 14389168, and the Marie Skłodowska-Curie grant No. 101104945.

-
- [1] M. C. Marchetti, J. F. Joanny, S. Ramaswamy, T. B. Liverpool, J. Prost, M. Rao, and R. A. Simha, Hydrodynamics of soft active matter, *Rev. Mod. Phys.* **85**, 1143 (2013).
- [2] C. Bechinger, R. Di Leonardo, H. Löwen, C. Reichhardt, G. Volpe, and G. Volpe, Active particles in complex and crowded environments, *Rev. Mod. Phys.* **88**, 045006 (2016).
- [3] É. Fodor and M. C. Marchetti, The statistical physics of active matter: From self-catalytic colloids to living cells, *Physica A* **504**, 106 (2018).
- [4] T. Vicsek, A. Czirók, E. Ben-Jacob, I. Cohen, and O. Shochet, Novel type of phase transition in a system of self-driven particles, *Phys. Rev. Lett.* **75**, 1226 (1995).
- [5] H. Chaté, Dry aligning dilute active matter, *Annu. Rev. Condens. Matter Phys.* **11**, 189 (2020).
- [6] Y. Fily and M. C. Marchetti, Athermal phase separation of self-propelled particles with no alignment, *Phys. Rev. Lett.* **108**, 235702 (2012).
- [7] M. E. Cates and J. Tailleur, Motility-induced phase separation, *Annu. Rev. Condens. Matter Phys.* **6**, 219 (2015).
- [8] A. Bailles, E. W. Gehrels, and T. Lecuit, Mechanochemical principles of spatial and temporal patterns in cells and tissues, *Annu. Rev. Cell Dev. Biol.* **38**, 321 (2022).
- [9] A. Karma, Physics of cardiac arrhythmogenesis, *Annu. Rev. Condens. Matter Phys.* **4**, 313 (2013).
- [10] K. M. Myers and D. Elad, Biomechanics of the human uterus, *WIREs Syst. Biol. Med.* **9**, e1388 (2017).
- [11] Y. Zhang and E. Fodor, Pulsating active matter, *Phys. Rev. Lett.* **131**, 238302 (2023).
- [12] E. Tjhung and T. Kawasaki, Excitation of vibrational soft modes in disordered systems using active oscillation, *Soft Matter* **13**, 111 (2017).
- [13] E. Tjhung and L. Berthier, Discontinuous zation transition in time-correlated assemblies of actively deforming particles, *Phys. Rev. E* **96**, 050601 (2017).
- [14] N. Oyama, T. Kawasaki, H. Mizuno, and A. Ikeda, Glassy dynamics of a model of bacterial cytoplasm with metabolic activities, *Phys. Rev. Research* **1**, 032038 (2019).
- [15] Y. Koyano, H. Kitahata, and A. S. Mikhailov, Diffusion in crowded colloids of particles cyclically changing their shapes, *EPL* **128**, 40003 (2019).
- [16] Y. Togashi, Modeling of nanomachine/micromachine crowds: Interplay between the internal state and surroundings, *J. Phys. Chem. B* **123**, 1481 (2019).
- [17] A. Manacorda and E. Fodor, Pulsating with discrete symmetry, ArXiv e-prints (2023), arXiv:2310.14370.
- [18] W. hua Liu, W. jing Zhu, and B. quan Ai, Collective motion of pulsating active particles in confined structures, *New J. Phys.* **26**, 023017 (2024).
- [19] Z.-Q. Li, Q.-L. Lei, and Y. qiang Ma, Fluidization and anomalous density fluctuations in epithelial tissues with pulsating activity, ArXiv e-prints (2024), arXiv:2402.02981.
- [20] R. L. Jack, Ergodicity and large deviations in physical systems with stochastic dynamics, *Eur. Phys. J. B* **93**, 74 (2020).
- [21] H. Touchette, The large deviation approach to statistical mechanics, *Phys. Rep.* **478**, 1 (2009).
- [22] J. P. Garrahan, R. L. Jack, V. Lecomte, E. Pitard, K. van Duijvendijk, and F. van Wijland, Dynamical first-order phase transition in kinetically constrained models of glasses, *Phys. Rev. Lett.* **98**, 195702 (2007).
- [23] N. Tizón-Escamilla, C. Pérez-Espigares, P. L. Garrido, and P. I. Hurtado, Order and symmetry breaking in the fluctuations of driven systems, *Phys. Rev. Lett.* **119**, 090602 (2017).
- [24] C. P. Royall, F. Turci, and T. Speck, Dynamical phase transitions and their relation to structural and thermodynamic aspects of glass physics, *J. Chem. Phys.* **153**, 090901 (2020).
- [25] R. Chetrite and H. Touchette, Nonequilibrium markov processes conditioned on large deviations, *Annales Henri Poincaré* **16**, 2005 (2015).
- [26] R. L. Jack and P. Sollich, Effective interactions and large deviations in stochastic processes, *Eur. Phys. J. Special Topics* **224**, 2351 (2015).
- [27] U. Ray, G. K.-L. Chan, and D. T. Limmer, Exact fluctuations of nonequilibrium steady states from approximate auxiliary dynamics, *Phys. Rev. Lett.* **120**, 210602 (2018).
- [28] L. Tociu, É. Fodor, T. Nemoto, and S. Vaikuntanathan, How dissipation constrains fluctuations in nonequilibrium liquids: Diffusion, structure, and biased interactions, *Phys. Rev. X* **9**, 041026 (2019).
- [29] A. Das and D. T. Limmer, Nonequilibrium design strategies for functional colloidal assemblies, *Proc. Natl. Acad. Sci. USA* **120**, e2217242120 (2023).
- [30] A. Lamtyugina, Y. Qiu, E. Fodor, A. R. Dinner, and S. Vaikuntanathan, Thermodynamic control of activity patterns in cytoskeletal networks, *Phys. Rev. Lett.* **129**, 128002 (2022).
- [31] E. Fodor, R. L. Jack, and M. E. Cates, Irreversibility and biased ensembles in active matter: Insights from stochastic thermodynamics, *Annu. Rev. Condens. Matter Phys.* **13**, 215 (2022).
- [32] F. Cagnetta, F. Corberi, G. Gonnella, and A. Suma, Large fluctuations and dynamic phase transition in a system of self-propelled particles, *Phys. Rev. Lett.* **119**, 158002 (2017).
- [33] S. Whitelam, K. Klymko, and D. Mandal, Phase separation and large deviations of lattice active matter, *J. Chem. Phys.* **148**, 154902 (2018).
- [34] T. GrandPre, K. Klymko, K. K. Mandadapu, and D. T. Limmer, Entropy production fluctuations encode collective behavior in active matter, *Phys. Rev. E* **103**, 012613 (2021).
- [35] T. Nemoto, E. Fodor, M. E. Cates, R. L. Jack, and J. Tailleur, Optimizing active work: Dynamical phase transitions, collective motion, and jamming, *Phys. Rev. E* **99**, 022605 (2019).
- [36] Y.-E. Keta, E. Fodor, F. van Wijland, M. E. Cates, and R. L. Jack, Collective motion in large deviations of active particles, *Phys. Rev. E* **103**, 022603 (2021).
- [37] T. Agranov, M. E. Cates, and R. L. Jack, Tricritical behavior in dynamical phase transitions, *Phys. Rev. Lett.* **131**, 017102 (2023).
- [38] See supplemental material at [URL_will_be_inserted_](#)

by_publisher.

- [39] B. Wittich and U. K. Deiters, The influence of the simulation box geometry in solid-state molecular simulations: phase behaviour of lithium iodide in a dynamic monte carlo simulation, *Mol. Simul.* **36**, 364 (2010).
- [40] G. Zhang, F. H. Stillinger, and S. Torquato, Probing the limitations of isotropic pair potentials to produce ground-state structural extremes via inverse statistical mechanics, *Phys. Rev. E* **88**, 042309 (2013).
- [41] W. D. Piñeros and T. M. Truskett, Designing pairwise interactions that stabilize open crystals: Truncated square and truncated hexagonal lattices, *J. Chem. Phys.* **146**, 144501 (2017).
- [42] C. Giardinà, J. Kurchan, and L. Peliti, Direct evaluation of large-deviation functions, *Phys. Rev. Lett.* **96**, 120603 (2006).
- [43] T. Nemoto, F. Bouchet, R. L. Jack, and V. Lecomte, Population-dynamics method with a multicanonical feedback control, *Phys. Rev. E* **93**, 062123 (2016).
- [44] R. Hurtado-Gutiérrez, F. Carollo, C. Pérez-Espigares, and P. I. Hurtado, Building continuous time crystals from rare events, *Phys. Rev. Lett.* **125**, 160601 (2020).
- [45] G. Briand, M. Schindler, and O. Dauchot, Spontaneously flowing crystal of self-propelled particles, *Phys. Rev. Lett.* **120**, 208001 (2018).
- [46] L. Berthier, E. Flenner, and G. Szamel, Glassy dynamics in dense systems of active particles, *J. Chem. Phys.* **150**, 200901 (2019).
- [47] R. Mandal, P. J. Bhuyan, P. Chaudhuri, C. Dasgupta, and M. Rao, Extreme active matter at high densities, *Nat. Commun.* **11**, 2581 (2020).
- [48] P. K. Morse, S. Roy, E. Agoritsas, E. Stanifer, E. I. Corwin, and M. L. Manning, A direct link between active matter and sheared granular systems, *Proc. Natl. Acad. Sci. USA* **118**, e2019909118 (2021).
- [49] E. Tjhung and L. Berthier, Analogies between growing dense active matter and soft driven glasses, *Phys. Rev. Res.* **2**, 043334 (2020).
- [50] A. Ninarello, L. Berthier, and D. Coslovich, Models and algorithms for the next generation of glass transition studies, *Phys. Rev. X* **7**, 021039 (2017).
- [51] C. Brito, E. Lerner, and M. Wyart, Theory for swap acceleration near the glass and jamming transitions for continuously polydisperse particles, *Phys. Rev. X* **8**, 031050 (2018).
- [52] M. L. Manning, Essay: Collections of deformable particles present exciting challenges for soft matter and biological physics, *Phys. Rev. Lett.* **130**, 130002 (2023).
- [53] H. Sakaguchi and Y. Kuramoto, A Soluble Active Rotator Model Showing Phase Transitions via Mutual Entertainment, *Prog. Theor. Phys.* **76**, 576 (1986).
- [54] K. P. O’Keeffe, H. Hong, and S. H. Strogatz, Oscillators that sync and swarm, *Nat. Commun.* **8**, 1504 (2017).
- [55] B. Adorjani, A. Libal, C. Reichhardt, and C. J. O. Reichhardt, Motility induced phase separation and frustration in active matter swarms, *ArXiv e-prints* (2023), [arXiv:2309.10937](https://arxiv.org/abs/2309.10937).
- [56] S. Whitelam, D. Jacobson, and I. Tamblyn, Evolutionary reinforcement learning of dynamical large deviations, *J. Chem. Phys.* **153**, 044113 (2020).
- [57] A. Das, D. C. Rose, J. P. Garrahan, and D. T. Limmer, Reinforcement learning of rare diffusive dynamics, *J. Chem. Phys.* **155**, 134105 (2021).
- [58] J. Yan, H. Touchette, and G. M. Rotskoff, Learning nonequilibrium control forces to characterize dynamical phase transitions, *Phys. Rev. E* **105**, 024115 (2022).

Supplemental material: Biased ensembles of pulsating active matter

William D. Piñeros and Étienne Fodor

Department of Physics and Materials Science, University of Luxembourg, L-1511 Luxembourg, Luxembourg

I. UNBIASED DYNAMICS

To highlight the effect of box geometry in constraining the unbiased dynamics, we illustrate in Fig. S1 the corresponding snapshots of the system at zero bias for values of L/ℓ which, under bias, induce cycles ($L/\ell = 4.13$) and arrest ($L/\ell = 5$). As seen, the system with $L/\ell = 5$ at $s = 0$ already features the regular structure of the corresponding packing observed upon bias, see also movies online. To further illustrate the relation between particle packing and box geometry, we compute the averaged overlap distance:

$$\langle \sigma_{ov} \rangle = \frac{1}{N_p} \sum_i \sum_{j>i} \langle (\sigma_j + \sigma_i - r_{ij}) H(\sigma_j + \sigma_i - r_{ij}) \rangle, \quad (S1)$$

where r_{ij} is the interparticle distance, $\sigma_{i/j}$ the respective particle radii, $N_p \equiv N(N-1)/2$ the number of unique pairs, and $H(\cdot)$ the Heaviside function. We compare $\langle \sigma_{ov} \rangle$ with the value σ_{ovx} for a perfect hexagonal lattice, for which particle sizes minimize the repulsion but induce dynamic arrest, see Appendix A. Simulations are carried out for 100 independent runs, and averaged over a trajectory length of $t = 200$ with time step $dt = 0.0005$. In Fig. S1, we show the resulting plot of $\langle \sigma_{ov} \rangle / \sigma_{ovx}$ against the aspect ratio L/ℓ and identify the following two results: 1) the maximum overlap falls closely within the same L/ℓ range that results in maximum order parameter and dynamic slowdown, as discussed in the main text [Fig. 2]; and 2) $\langle \sigma_{ov} \rangle / \sigma_{ovx}$ is closer to unity near the maximum showing that some box ratios can result in effective system repulsion approaching that of the arrested hexagonal packing limit. Therefore the overall effect of box geometry may be understood as a constraint on packing configurations with some values of L/ℓ inducing tighter, more repulsive particle arrangements than others.

II. BIASED DYNAMICS

A. Control interactions for bias with global order

Adding control interactions in the dynamics is a generic strategy to improve the sampling of biased ensembles (BEs). We discuss in this section how to adapt the trajectory selection accordingly. For the unbiased dynamics

$$\dot{\mathbf{r}}_i = -\mu_r \partial_{\mathbf{r}_i} V + \sqrt{2D_r} \boldsymbol{\xi}_i, \quad \dot{\theta}_i = \omega - \mu_\theta \partial_{\theta_i} V + \sqrt{2D_\theta} \eta_i, \quad (S2)$$

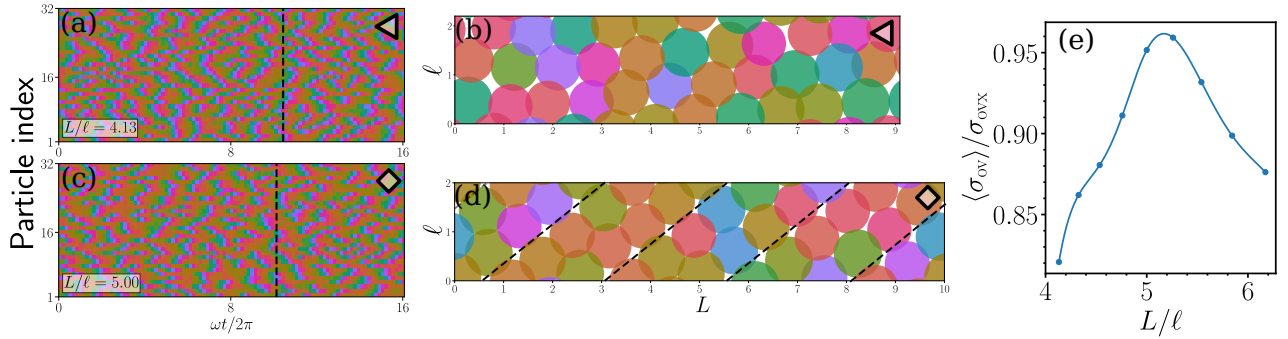


FIG. S1. (a,b) Trajectory of unbiased dynamics and (c,d) corresponding snapshots at the time denoted by the vertical dashed line: the case $L/\ell = 5$ displays a regular packing configuration. (e) Average particle overlap $\langle \sigma_{ov} \rangle$ as a function of the aspect ratio L/ℓ , where σ_{ovx} is the overlap for a perfect hexagonal lattice at the same density. Solid line is a cubic spline fit between data points. Parameters: $N = 32$, $\rho = 1.6$.

the probability to observe a trajectory for $\{\mathbf{r}_i, \theta_i\}$ within a time interval $[0, t_o]$ is given in terms of the path weight $\mathcal{P}[\{\mathbf{r}_i, \theta_i\}_0^{t_o}] \sim e^{-\mathcal{A}_r - \mathcal{A}_\theta}$, where

$$\begin{aligned} \mathcal{A}_r &= \frac{1}{4D_r} \int_0^{t_o} dt \sum_{i=1}^N (\dot{\mathbf{r}}_i + \mu_r \partial_{\mathbf{r}_i} V)^2 - \frac{\mu_r}{2} \int_0^{t_o} dt \sum_{i=1}^N \partial_{\mathbf{r}_i}^2 V, \\ \mathcal{A}_\theta &= \frac{1}{4D_\theta} \int_0^{t_o} dt \sum_{i=1}^N (\dot{\theta}_i - \omega + \mu_\theta \partial_{\theta_i} V)^2 - \frac{\mu_\theta}{2} \int_0^{t_o} dt \sum_{i=1}^N \partial_{\theta_i}^2 V. \end{aligned} \quad (\text{S3})$$

For the dynamics with the fully-connected synchronizing interaction

$$\dot{\theta}_i = \omega - \mu_\theta \partial_{\theta_i} V + \varepsilon \sum_{j=1}^N \sin(\theta_j - \theta_i) + \sqrt{2D_\theta} \eta_i, \quad (\text{S4})$$

the probability to observe a trajectory for $\{\mathbf{r}_i, \theta_i\}$ within a time interval $[0, t_o]$ is given in terms of the path weight $\mathcal{P}_{\text{gb}}[\{\mathbf{r}_i, \theta_i\}_0^{t_o}] \sim e^{-\mathcal{A}_r - \mathcal{A}_{\theta, \text{gb}}}$, where

$$\mathcal{A}_{\theta, \text{gb}} = \frac{1}{4D_\theta} \int_0^{t_o} dt \sum_{i=1}^N \left[\dot{\theta}_i - \omega + \mu_\theta \partial_{\theta_i} V - \varepsilon \sum_{j=1}^N \sin(\theta_j - \theta_i) \right]^2 - \frac{1}{2} \int_0^{t_o} dt \sum_{i=1}^N \partial_{\theta_i} \left[\mu_\theta \partial_{\theta_i} V - \varepsilon \sum_{j=1}^N \sin(\theta_j - \theta_i) \right]. \quad (\text{S5})$$

To ensure that we sample the same BE with and without control interaction, the biasing observable must be modified with respect to the control interaction. For example, for the ensemble biased with global order [Eq. (7) in main text], we define the biasing observable $\hat{\phi}_{\text{gb}}$ by ensuring that the biased path weight is the same with and without control:

$$\mathcal{P}[\{\mathbf{r}_i, \theta_i\}_0^{t_o}] e^{-sNt_o \bar{\phi}_{\text{gb}}} = \mathcal{P}_{\text{gb}}[\{\mathbf{r}_i, \theta_i\}_0^{t_o}] e^{-sNt_o \hat{\phi}_{\text{gb}}}. \quad (\text{S6})$$

Combining Eqs. (S3), (S5) and (S6) provides an explicit expression for $\hat{\phi}_{\text{gb}}$. Note that this procedure holds for *any* value of ε , including $\varepsilon = 0$. This grants us an additional degree of freedom with which to improve BE convergence. Here, we adopt a strategy that relates the level of chosen bias s to the strength of the control force ε via a relation in the observable $\bar{\phi}_{\text{gb}}$. In particular for a given s we choose ε such that

$$\langle \bar{\phi}_{\text{gb}}(s) \rangle_{\text{gb}} = \langle \bar{\phi}_{\text{gb}}(\varepsilon) \rangle_{\text{con}}, \quad (\text{S7})$$

where $\langle \cdot \rangle_{\text{gb}}$ denote the biased, controlled ensemble average and $\langle \cdot \rangle_{\text{con}}$ the *unbiased*, controlled ensemble respectively. In practice, we evaluate $\langle \bar{\phi}_{\text{gb}}(\varepsilon) \rangle_{\text{con}}$ numerically over a range of values and use the resulting function as a calibration curve with which to invert for the optimal ε given a value of s . In the population dynamics algorithm, the update of ε is implemented throughout the trajectory, until ε converges to a stationary value. A similar strategy has been employed successfully in other BE studies [S1, S2].

As a demonstration, we test our expression for $\hat{\phi}_{\text{gb}}$ by comparing two numerical evaluations, with and without control, of the scaled cumulant generating function (SCGF):

$$\psi_{\text{gb}} = \frac{1}{Nt_o} \ln \langle e^{-sNt_o \bar{\phi}_{\text{gb}}} \rangle. \quad (\text{S8})$$

To this end, we consider a smaller, less dense system of $N = 11$ particles at density $\rho = 1.2$ than the one studied in the main text. This choice allows us to ensure convergence even without control forces, thus serving as a comparison with the results obtained with control forces. It also illustrates how control interactions accelerate sampling by reducing computational effort, here estimated by the number of clones n_c used to arrive at converged solutions. As reported in Figs. S2(a-b), values of ψ sampled either with or without show excellent agreement, but almost by an order of magnitude in reduced computational effort ($n_{c, \text{noncon}}/n_{c, \text{con}} = 1/8$) with control. For all our numerical results, presented here and in the main text, we therefore use control interaction with $n_c = 10000$.

B. Control interactions for bias with local order

When biasing with local order [Eq. (10) in main text], we also consider control interaction promoting local synchronization:

$$\dot{\theta}_i = \omega - \mu_\theta \partial_{\theta_i} V + \varepsilon \sum_{j=1}^{n_i} \sin(\theta_j - \theta_i) + \sqrt{2D_\theta} \eta_i, \quad (\text{S9})$$

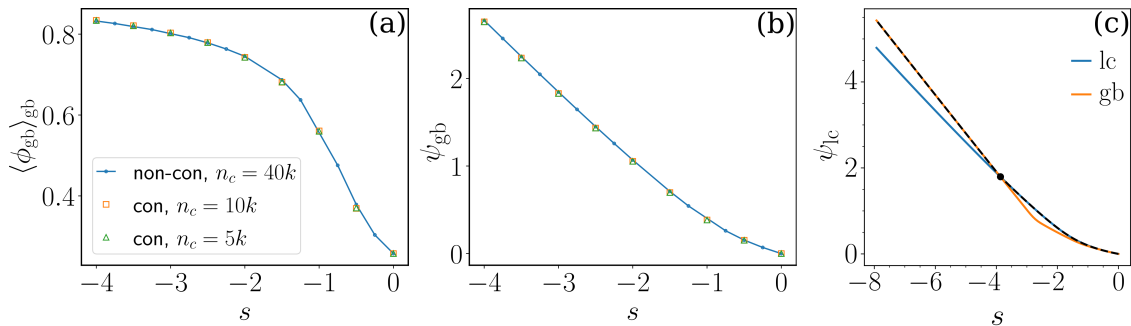


FIG. S2. Ensemble biased by global order [Eq. (7) in main text]: (a) global order $\langle \phi_{gb} \rangle_{gb}$ and (b) scaled cumulative generating function ψ_{lc} as functions of the bias strength s . Blue dotted line is without control interaction and with $n_c = 40000$ clones. Orange squares and green triangles denote data control interaction f_c and with $n_c = 5000$ and $n_c = 10000$, respectively. Parameters: $N = 11$, $\rho = 1.2$, $t_o = 16000$. Ensemble biased by local order [Eq. (10) in main text]: (c) scaled cumulative generating function ψ_{lc} as a function of the bias strength s , sampled with either global or local control interactions in orange and blue lines, respectively. Best estimate of ψ_{lc} is shown in the dashed line. Parameters: $N = 32$, $\rho = 1.6$ and $L/\ell = 1.9$

where n_i is the number of neighbors in contact with particle i , and for which the probability to observe a trajectory for $\{\mathbf{r}_i, \theta_i\}$ within a time interval $[0, t_o]$ is given in terms of the path weight $\mathcal{P}_{lc}[\{\mathbf{r}_i, \theta_i\}_0^{t_o}] \sim e^{-\mathcal{A}_r - \mathcal{A}_{\theta,lc}}$, where

$$\mathcal{A}_{\theta,lc} = \frac{1}{4D_\theta} \int_0^{t_o} dt \sum_{i=1}^N \left[\dot{\theta}_i - \omega + \mu_\theta \partial_{\theta_i} V - \varepsilon \sum_{j=1}^{n_i} \sin(\theta_j - \theta_i) \right]^2 - \frac{1}{2} \int_0^{t_o} dt \sum_{i=1}^N \partial_{\theta_i} \left[\mu_\theta \partial_{\theta_i} V - \varepsilon \sum_{j=1}^{n_i} \sin(\theta_j - \theta_i) \right]. \quad (\text{S10})$$

As before, for either the fully-connected [Eq. (S4)] or locally [Eq. (S9)] synchronizing interactions, we define the biasing observable $\hat{\phi}_x$, where $x \in \{lc, gb\}$ respectively for each force, by ensuring that the biased path weight is the same with and without control:

$$\mathcal{P}[\{\mathbf{r}_i, \theta_i\}_0^{t_o}] e^{-sNt_o \bar{\phi}_{lc}} = \mathcal{P}_x[\{\mathbf{r}_i, \theta_i\}_0^{t_o}] e^{-sNt_o \hat{\phi}_x}. \quad (\text{S11})$$

We compare the convergence for either one of the control interactions by considering the SCGF with respect to local order and the respective choice of control force:

$$\psi_{lc,x} = \frac{1}{Nt_o} \ln \langle e^{-sNt_o \bar{\phi}_{lc}} \rangle_x. \quad (\text{S12})$$

The SCGF $\psi_{lc,x}$ may display non-convex behavior near a dynamical phase transition, which is challenging to detail numerically. Given that $\langle \bar{\phi}_{lc}(s) \rangle = -\frac{d\psi(s)}{ds}$, we may also recast the expression of the SCGF as

$$\psi_{lc,x} = - \int_0^s \langle \bar{\phi}_{lc}(s') \rangle_x ds', \quad (\text{S13})$$

which is known to provide a smoother estimate of the SCGF from calculation of $\langle \bar{\phi}_{lc}(s) \rangle_x$ in the algorithm [S3].

While in principle either type of interaction (i.e., local or global) provides similar results in the limit of large t_o and large n_c , a particular choice may nonetheless best approximate the large deviation mechanism for the same amount of computational effort. This latter property is equivalent to choosing the sampling method that maximizes the value of ψ for any given value of s . We show in Fig. S2(c) that local interaction provides better estimates (namely larger values) of ψ_{lc} at small s , while global interaction works best at high s . In the main text, Fig. 4 thus reflects the best estimate of the phase diagram given the optimal choice of the control force for a given s and L/ℓ .

C. Packing structure under bias

To further illustrate the packing conditions of the pulsating particle system of the main text at high bias, we calculate its radial distribution function.

$$g(d) = (1/N) \sum_{i,j \neq i} \langle \delta(d - |\mathbf{d}_i - \mathbf{d}_j|) \rangle, \quad (\text{S14})$$

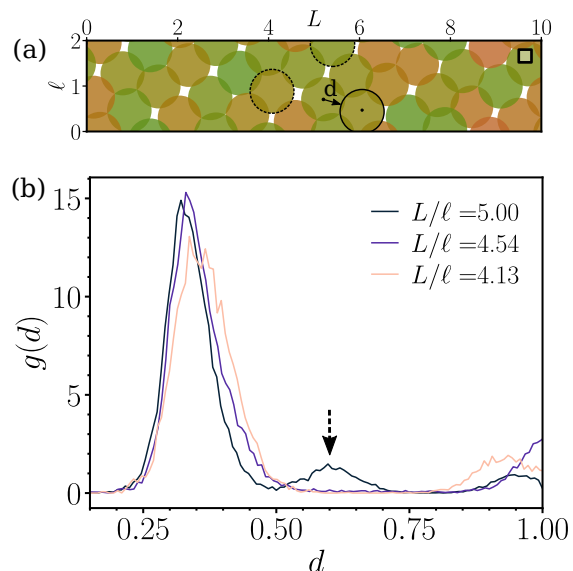


FIG. S3. (a) Snapshot of the biased system ($N = 32$, $\rho = 1.6$) in the main text at high bias ($s = -6$). Here \mathbf{d} denotes the vector connecting the center-of-mass distance to that of its closest-neighbors particle face. (b) Corresponding radial distribution of $d = |\mathbf{d}|$ for the three biased systems $L/\ell = \{5, 4.54, 4.13\}$ represented in Figs. 1(b-d) of the main text. The dashed arrow corresponds to the particles with dashed boundaries in panel (a), which represent the second-nearest neighbors of that packing configuration ($L/\ell = 5$).

where we define d as the center-of-mass to particle *face* distance [see Fig. S3(a)] and dimensionalized by σ_0 , the base particle size. This measure is advantageous over the traditional center-to-center distance in that it allows us to estimate particle coordination order beyond the radial constraint $r_{\max} = \min(\ell/2, L/2)$. The resulting $g(d)$ is shown in Fig. S3(b) for the states shown in Figs. 1(b-d) of the main text: $L/\ell = 5$ (arrested state), 4.54 (intermittent state), and 4.13 (cycling state). To compare packing configurations of approximately the same size distribution for all states, we average over configurations whose size distribution is within one standard deviation from that of the arrested state.

The curve for $L/\ell = 5$ (arrested state) has a sharp first peak, and also a correspondingly smaller second peak at $d \approx 0.6$ not present in the other two states. These peaks correspond, respectively, to the first and second nearest neighbors, the latter of which represent only two particles (hence the smaller peak) for this particular packing order. The curve for $L/\ell = 4.13$ (cycling state) has a first peak which is significantly broader than that of the other states. Such a broadening results from a wider distribution of average first shell distances, and hence points at a reduced rigidity due to defective packing. For the intermittent state ($L/\ell = 4.54$), the void in its structure causes neighbor swaps that broaden the first peak somewhat relative to that of the arrested state.

D. Phase diagram with $N = 26$ and $\rho = 1.6$

To highlight the impact of the box geometry on the emergent dynamics, we obtain the phase diagram of a system at the same density $\rho = 1.6$ as in the main text, yet at different particle number $N = 26$ ($N = 32$ in the main text) and box geometries L/ℓ . First, we measure in the unbiased dynamics $\langle \phi_{\text{gb}} \rangle$ and $\langle \nu \rangle$ as functions of L/ℓ [Figs. S4(a-b)]. Increasing high order systematically comes with decreasing current, as in the main text. Yet, this effect is here a lot sharper with distinct local maxima/minima, highlighting the highly non-monotonic effect of L/ℓ . As in the main text, regimes of relatively high order and low current at $s = 0$ result in arrested states upon bias [Figs. S4(c-d)]. Moreover, we again observe for large bias a transition between cycles and arrest, when changing L/ℓ at fixed s , which mirrors the slowdown of the unbiased dynamics.

Appendix A: Contact distance in dense monodisperse systems

We now explain how the maximum contact distance for a monodisperse crystal system is found. The number density ρ_h for hard discs of diameter l in a perfect hexagonal lattice (close packing) is $\rho_h = \sqrt{\frac{2}{\sqrt{3}}} \frac{1}{l^2}$, so that for $\rho > \rho_h$

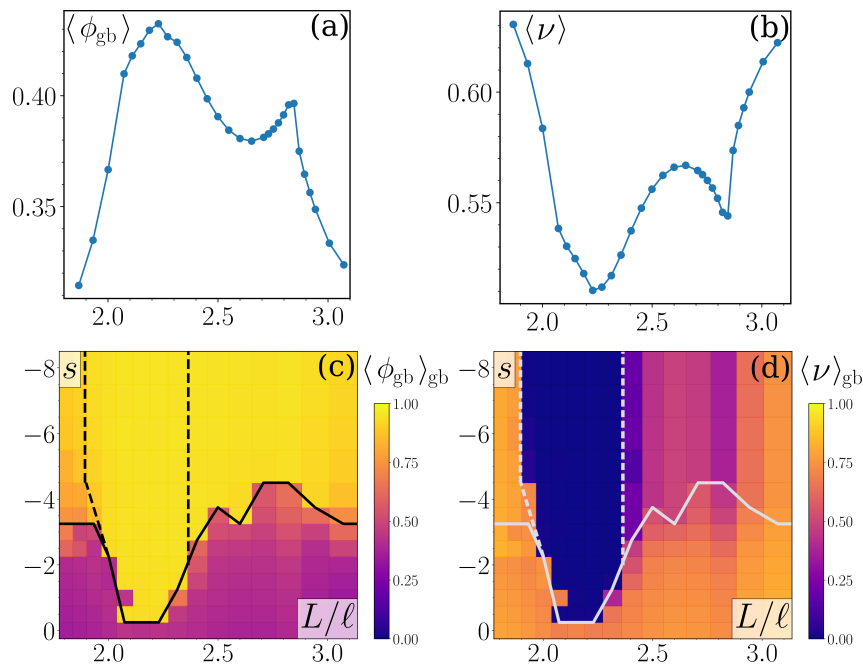


FIG. S4. (a-b) Global order $\langle \phi_{\text{gb}} \rangle$ and phase current $\langle \nu \rangle$ as functions of the aspect ratio L/ℓ in the unbiased dynamics. (c-d) Phase diagram in ensembles biased by global order [Eq. (7) in main text], in terms of global order $\langle \phi_{\text{gb}} \rangle_{\text{gb}}$ and current $\langle \nu \rangle_{\text{gb}}$ as functions of the bias strength s and the aspect ratio L/ℓ . Boundary lines are for $\langle \phi_{\text{gb}} \rangle_{\text{gb}} = 0.65$ (solid) and $\langle \nu \rangle_{\text{gb}} = 0.1$ (dashed). Parameters: $N = 26$, $\rho = 1.6$.

particles will overlap. The minimum particle diameter possible in our system is $\sigma_0 \frac{1-\lambda}{1+\lambda} \approx 0.905$, for which $\rho_h \approx 1.41$. Densities in our study are taken as $\rho \geq 1.55$, hence particles will always overlap. Minimizing the repulsion term is equivalent to finding the *maximum* interparticle distance r_m i.e. that with least particle overlap. Monodispersity implies that all particles have the same phase $\theta_i = \theta$. For arrested states, we get $\omega = n_n \mu_\theta \partial_\theta U(r, \theta)$, where n_n is the number of contact neighbors: this relation defines an implicit function $r = r(\theta, n_n)$. Assuming hexagonal packing, $n_n = 6$, and maximizing with respect to θ , we find $\theta_m = 0.562$ and $r(\theta_m, n_n) = 0.845$. The overlap distance follows as $\sigma_{\text{ovx}} = 2\sigma_m - r_m \approx 0.133$, where $\sigma_m = \frac{\sigma_0}{2} \frac{1+\lambda \sin(\theta_m)}{1+\lambda}$ is the optimal particle radius.

DATA AND CODE AVAILABILITY

Data of figures and plots in the main text are freely available in the Zenodo data repository at

<https://doi.org/10.5281/zenodo.10999011>

Code necessary to perform and replicate calculations of pulsating active matter in biased ensembles is available at:

https://github.com/CreditDefaultSwap/pulsating_active_matter_popdyn

-
- [S1] T. Nemoto, E. Fodor, M. E. Cates, R. L. Jack, and J. Tailleur, Optimizing active work: Dynamical phase transitions, collective motion, and jamming, *Phys. Rev. E* **99**, 022605 (2019).
[S2] Y.-E. Keta, E. Fodor, F. van Wijland, M. E. Cates, and R. L. Jack, Collective motion in large deviations of active particles, *Phys. Rev. E* **103**, 022603 (2021).
[S3] V. Lecomte and J. Tailleur, A numerical approach to large deviations in continuous time, *Journal of Statistical Mechanics: Theory and Experiment* **2007**, P03004 (2007).